JM PAPERS

Vibration-induced morphological evolution of a melting solid under microgravity

Wen-Ping Fang[1,‡], **Jian-Zhao Wu**[1,2,‡], **Ze-Lin Huang**[1], **Bo-Fu Wang**[1], **Quan Zhou**[1] **and Kai Leong Chong**[1,2,†]

[1]Shanghai Key Laboratory of Mechanics in Energy Engineering, Shanghai Institute of Applied Mathematics and Mechanics, School of Mechanics and Engineering Science, Shanghai University, Shanghai 200072, PR China

[2]Shanghai Institute of Aircraft Mechanics and Control, Zhangwu Road, Shanghai 200092, PR China

We study the melting process of a solid under microgravity, driven solely by lateral vibrations that are perpendicular to the applied temperature gradient due to the absence of gravity-induced convection. Using direct numerical simulations with the phase-field method, we examine two-dimensional vibration-induced melting in a square cavity over four orders of magnitude of vibrational Rayleigh numbers, $10^5 \leq Ra_{vib} \leq 10^9$. Our results show that as melting progresses, the flow structure transitions from a periodic-circulation regime with diffusion-dominated heat transfer to a columnar regime with vibroconvection. The mean height of the liquid–solid interface follows a power-law dependency with time, $\bar{\xi} \sim \tilde{t}^{1/(2-2\alpha)}$, where $\alpha = 0$ in the periodic-circulation regime and $\alpha = 1/2$ in the columnar regime. We further observe that within the columnar regime, the morphological evolution of the liquid–solid interface is influenced by the interaction of columnar thermal plumes in the central regions and the peripheral flow near the sidewalls. Specifically, we offer a comprehensive analysis of the plume merging behaviour, which is governed by the aspect ratio ($\bar{\xi}$) of the liquid layer and the intensity of vibration, quantified by the effective vibrational Rayleigh number Ra_{vib}^{eff}. We identify the relationship between the number of columnar plumes K_m and Ra_{vib}^{eff}, finding that $K_m \sim \bar{\xi}^{-1}(Ra_{vib}^{eff})^{\gamma}$ with the fitting scaling exponent $\gamma = 0.150 \pm 0.025$. We subsequently quantify the characteristics of the interface roughness amplitude evolution in microgravity vibroconvection. Our results indicate that the roughness amplitude exhibits a power-law dependence on the mean height of the liquid layer. Drawing from the Stefan boundary condition, we theoretically deduce this dependence under the assumption of a non-uniform heat flux distribution at the interface, where the theory is corroborated by our numerical simulations.

Key words: solidification/melting

---

† Email address for correspondence: klchong@shu.edu.cn
‡ These authors contributed equally to this work.

W.-P. Fang, J.-Z. Wu, Z.-L. Huang, B.-F. Wang, Q. Zhou and K.L. Chong

1. Introduction

The liquid–solid phase transition process, characterized by the evolution of a moving interface, is a common phenomenon in geophysics, astrophysics and various industrial applications. Notable examples include glacier melting (Hock 2005), solidification of magma chambers (Thomas, Cassoni & MacArthur 1996), aircraft de-icing (Thomas *et al.* 1996), the dynamics of magma oceans (Ulvrová *et al.* 2012) and the melting of phase-change materials (PCMs) (Raoux 2009). In all these examples, gravity plays a pivotal role in influencing the liquid–solid phase transition (Li *et al.* 2017), primarily because buoyancy significantly affects the heat transfer dynamics that is central to the phase-change process.

In geophysical applications on Earth, where gravity is present, various numerical methods have been employed to investigate the impact of factors such as buoyancy, rotation, shear, turbulence and meltwater plumes on the morphological evolution of the liquid–solid interface (Favier, Purseed & Duchemin 2019; Couston *et al.* 2021; Ravichandran & Wettlaufer 2021; Wilson *et al.* 2023; Yang *et al.* 2023*b*). These studies have also examined the effects of aspect ratio (Hester *et al.* 2021), solid shape (Yang *et al.* 2024), density anomalies (Wang *et al.* 2021; Yang *et al.* 2022) and salinity on the melting process (Du *et al.* 2023; Yang *et al.* 2023*a*) and the bistability property of melting (Purseed *et al.* 2020). Additionally, experimental studies have been conducted to uncover the underlying physics of these phenomena (Davis, Müller & Dietsche 1984; FitzMaurice, Cenedese & Straneo 2017; Bushuk *et al.* 2019; Wang *et al.* 2021).

It is worth noting that liquid–solid phase transitions also have industrial significance, particularly in latent heat energy storage devices utilizing PCMs. Previous studies have examined how the roughness of the basic morphology of PCMs affects heat transfer efficiency and thus the melting rate (Kamkari & Amlashi 2017). Most studies have focused on the interplay between buoyancy-driven flow and the evolution of the melting interface. However, there is an increasing demand for harnessing PCMs in microgravity environments, such as in microscale devices (Glicksman, Lupulescu & Koss 2003; Chen *et al.* 2019) or devices used in space missions. In microgravity, due to the minimal flow occurring in the liquid zone, the melting process is predominantly driven by thermal conduction, leading to a relatively slow melting rate. For the application of PCMs in microgravity, several studies have been conducted, including enhancing effective thermal diffusivity with nano-enhanced PCMs (Hosseinizadeh, Darzi & Tan 2012; Dhaidan *et al.* 2013), using thermocapillary-driven flow (Sánchez *et al.* 2020*a*, 2021; Šeta *et al.* 2023) and adjusting the positions of heat sources and sinks (Mahmud & Ahmed 2022). In this work, we demonstrate the potential of using vibration to achieve a superior melting rate in microgravity through vibration-induced convective flow.

Vibroconvection has been shown to be a promising method for driving convective flow and enhancing heat transfer (Gershuni & Lyubimov 1998; Mialdun *et al.* 2008; Shevtsova *et al.* 2010; Guo *et al.* 2024*b*; Huang *et al.* 2024). Numerous studies have investigated the interaction between vibroconvection and buoyancy-driven convection (Wang, Zhou & Sun 2020; Guo *et al.* 2022; Wu *et al.* 2022*a*; Wu, Wang & Zhou 2022*b*), demonstrating the potential of vibration to perturb boundary layers and modulate heat flux. One crucial factor is the relative orientation of the vibrational axis and the temperature gradient (Demin, Gershuni & Verkholantsev 1996; Cissé, Bardan & Mojtabi 2004). When the vibration direction is perpendicular to the temperature gradient, dynamic destabilization of thermal convection occurs, significantly enhancing heat transfer (Wang *et al.* 2020; Wu *et al.* 2021). In contrast, when the vibration direction is parallel to the temperature gradient, dynamic

stabilization of convective flows results in the suppression of convective heat transfer (Carbo, Smith & Poese 2014; Wu *et al.* 2022*a*). Recently, works by Rahmanian *et al.* (2023) and Guo *et al.* (2024*a*) applied vibration to the problem of PCMs, and their studies demonstrated that the performance of PCM thermal energy storage units can be improved by using a small oscillator plate. They validated the effectiveness and cost-efficiency of this method through numerical analysis.

In microgravity environments, there has been growing interest in studying thermal convection solely driven by vibrations. Vibrations in microgravity can be generated by structural resonances, the operation of spacecraft mechanical systems and astronaut activities. Experimental studies on vibroconvection date back to the Apollo spacecraft missions (Bannister *et al.* 1973), where vibrations were found to significantly increase heat transfer compared to pure conduction (Grodzka & Bannister 1975). Subsequent experimental study has shown that external vibrations can significantly affect thermal diffusion processes (Garrabos *et al.* 2007; Braibanti *et al.* 2019). Shevtsova *et al.* (2010) conducted experiments on the flow structure and heat transfer of vibroconvection in a low-gravity environment during parabolic flights, finding that increased vibration intensity significantly enhanced heat transfer via streaming flow. More recently, Guo *et al.* (2023) and Huang *et al.* (2024) revealed unified constitutive laws of heat transport and the transition of flow structure in microgravity vibroconvection. In addition, Sánchez *et al.* (2019, 2020*b*) extended the study by exploring instabilities in miscible and immiscible fluids under microgravity, focusing on how external vibrational excitation can control dynamic interface behaviour and pattern selection. This highlights the broader relevance of vibrations not only for heat transfer but also for fluid interface management in space. Porter *et al.* (2021) reviewed these developments, emphasizing the potential for controlling fluid instabilities in microgravity.

The previous studies show that, in microgravity environments, vibroconvection is an effective means of enhancing heat transfer efficiency. When vibroconvection is applied to drive the melting process in microgravity, it raises a crucial question: how does vibroconvection affect the morphological evolution of the melting interface? To address this question, we conducted direct numerical simulations of a solid melting in a two-dimensional square cavity subjected to an external temperature difference and vibration, studying the morphology evolution of the melting process driven by vibroconvection under microgravity conditions. The remainder of the article is structured as follows. In § 2, we present the governing equations and numerical set-up. In § 3, we examine the effect of vibroconvection on the evolution of the interface height. In § 4, we investigate the influences of the merging of columnar plumes and peripheral flow near sidewalls. In § 5, we analyse the evolution of the interface roughness amplitude. Finally, we provide a brief conclusion and outlook in § 6.

2. Governing equations and problem set-up

We consider the evolution of a melting solid in a square heated from below as shown in figure 1. The square is bounded by four impenetrable, no-slip walls with a size of H. We adopt a constant temperature $T = T_h$ on the bottom plate and $T = T_m$ on the top plate with T_m being the melting temperature and $T_h < T_m$. As gravity is absent in microgravity, a horizontal harmonic vibration $A \cos(\Omega t)\boldsymbol{e}_x$ is imposed to act as an artificial driving (Beysens 2006), which generates vibroconvection (Gershuni & Lyubimov 1998; Shevtsova *et al.* 2010; Huang *et al.* 2024) driving the melting process. Associated with the vibration, an inertial acceleration of $A\Omega^2 \cos(\Omega t)\boldsymbol{e}_x$ perpendicular to the temperature gradient is

introduced into the system. Here, A is the vibration amplitude, Ω is the vibration frequency and $\boldsymbol{e}_x$ is the unit vector in the x direction. We employed the phase-field method (Hester *et al.* 2020) to simulate the melting of the solid. In this approach, a phase-field value of $\phi = 1$ represents the solid phase, while $\phi = 0$ represents the liquid phase. Therefore, the melting system is governed by the incompressible Navier–Stokes equations under the Oberbeck–Boussinesq approximation in addition to the dynamic equation of the phase field ϕ. Non-dimensionalized by the cell size H, the characteristic velocity $\beta \Delta A \Omega$ and the temperature difference $\Delta = T_h - T_m$, the non-dimensional governing equations for this system read

$$\frac{\partial u_i}{\partial t} + u_j \frac{\partial u_i}{\partial x_j} = -\frac{\partial p}{\partial x_i} - a^{-1} \cos(a^{-1}t)\theta\delta_{1i} + \sqrt{\frac{Pr}{2Ra_{vib}}} \frac{\partial^2 u_i}{\partial x_j \partial x_j} - \frac{\phi u_i}{\eta}, \qquad (2.1)$$

$$\frac{\partial \theta}{\partial t} + u_j \frac{\partial \theta}{\partial x_j} = \frac{1}{\sqrt{2Ra_{vib}Pr}} \frac{\partial^2 \theta}{\partial x_j \partial x_j} + St\frac{\partial \phi}{\partial t}, \qquad (2.2)$$

$$\frac{\partial \phi}{\partial t} = \frac{6}{5CSt\sqrt{2Ra_{vib}Pr}} \left[\frac{\partial^2 \phi}{\partial x_j \partial x_j} - \frac{1}{\epsilon^2}\phi(1-\phi)(1-2\phi+C\theta) \right], \qquad (2.3)$$

with the incompressibility constraint $\partial u_i/\partial x_i = 0$. Here, u_i ($\equiv (u, w)$) is the dimensionless fluid velocity, p is the dimensionless pressure and $\theta = (T - T_m)/\Delta$ is the dimensionless temperature. In (2.1), η is the velocity penalty parameter and set equal to the time step (Yang *et al.* 2023*b*). In (2.3), ϵ represents the dimensionless thickness of the diffusive interface and is set equal to the grid spacing (Favier *et al.* 2019); C is a parameter that controls the extent of curvature impact on the melting point at the interface and $C = 1$ is adopted due to the relatively small local curvature (Couston *et al.* 2021; Yang *et al.* 2023*b*). In this system, there are four control parameters, namely the vibrational Rayleigh number Ra_{vib}, the Prandtl number Pr, the Stefan number St and the non-dimensional vibration amplitude a:

$$Ra_{vib} = \frac{(\beta A\Omega \Delta H)^2}{2\nu\kappa}, \quad Pr = \frac{\nu}{\kappa}, \quad St = \frac{\mathcal{L}}{c_p\Delta}, \quad a = \frac{\beta A\Delta}{H}, \qquad (2.4a\text{--}d)$$

where ν is the kinematic viscosity coefficient of the liquid, κ is the thermal diffusivity coefficient (considered a constant and assumed to be equal in both phases), β is the thermal expansion coefficient, $\mathcal{L}$ denotes the latent heat and c_p is the specific heat capacity at constant pressure.

We note that for the boundary conditions of the velocity field, all solid walls are non-penetrable and non-slip, i.e. $u = 0$ and $w = 0$; for boundary conditions of the temperature field, constant temperatures are set on the top and bottom plates, i.e. $\theta = 1$ on bottom plates and $\theta = 0$ on top plates, while the sidewalls are adiabatic, i.e. $\partial_n\theta = 0$. At the liquid–solid interface, the heat flux balance theoretically follows the classical Stefan condition, which is written in dimensionless form:

$$Stu_n = \frac{1}{\sqrt{2Ra_{vib}Pr}}(\partial_n\theta^{(S)} - \partial_n\theta^{(L)}), \qquad (2.5)$$

where u_n is the normal velocity of the liquid–solid interface and the superscripts S and L respectively represent the solid and liquid phases. This Stefan condition (2.5) at the liquid–solid interface has been taken into account in the phase-field method (Favier *et al.* 2019; Hester *et al.* 2020). For the initial condition, we set a liquid layer with a small height
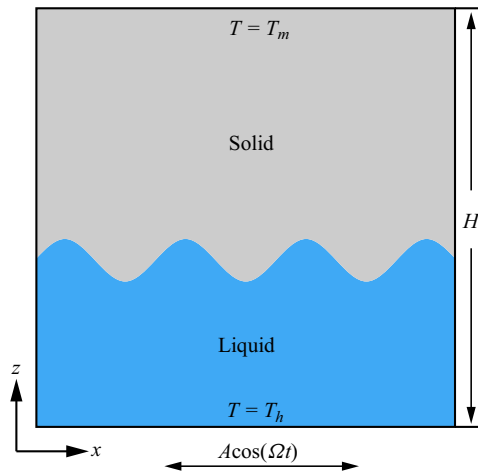
1001 A43-4

Figure 1. Sketch of vibration-induced a solid melting under microgravity conditions in a square cell with the coordinate systems. Lateral vibration is applied to generate convective flow driving the solid melting, and the vibration is perpendicular to the applied temperature gradient.

of $0.01H$ and a solid layer for other regions. The initial temperature of the solid phase is set equal to the temperature of the top plate ($\theta = 0$), while a linear temperature profile is assigned within the liquid phase. The initial velocity field is set to $u = 0$ and $w = 0$. With this configuration, the solid undergoes melting from the bottom upwards until complete liquefaction.

We carried out a series of direct numerical simulations to investigate the morphology evolution of a solid melting in microgravity. The governing equations (2.1)–(2.3) of this system are solved using a second-order finite-difference solver, which has been well validated in our previous studies (Wang *et al.* 2020; Guo *et al.* 2023; Yang *et al.* 2023*b*, 2024). And our numerical code has been adopted in simulating several problems of single-phase and multiphase turbulent flows (Zhao *et al.* 2022*a*,*b*; Huang *et al.* 2023; Chong *et al.* 2024; Meng *et al.* 2024; Zhang & Zhou 2024; Zhao *et al.* 2024). In all runs, we fix the Prandtl number at $Pr = 10$ for numerical convenience. Note that organic PCMs have high Prandtl numbers, while metals have very low Prandtl numbers. For water, the density anomaly at $4\,^\circ$C should be considered (Wang *et al.* 2021; Yang *et al.* 2022). First, *St* is fixed to 0.1, and we set $a = 0.01$ and vary Ra_{vib} from 10^5 to 10^9, corresponding to the heat transport mechanism in the thermal-boundary-layer-dominant regime reported in our previous work (Huang *et al.* 2024). The choice of *St* and a is made for computational efficiency, and we will discuss the potential effects when considering other values of a and *St* to apply to a broader range of PCMs and vibration sources. To accurately resolve the vibration-induced Stokes layer, we refined the mesh in the near-wall region and ensured a minimum of 16 grids within the Stokes layer under high-intensity vibration. The chosen time step, Δt, ensures at least 60 steps per a vibration period. More details of numerical parameters for all runs are given in table 1.

3. The evolution of mean height of liquid–solid interface

First, we investigate the temporal evolution of the height of the liquid–solid interface for vibration-induced melting in microgravity. Figure 2 depicts the spatio-temporal evolution of the interface height $\xi(x, t)$ for different Ra_{vib}. Here, the value of dimensionless height

Ra_{vib}	a	St	$N_x \times N_z$	Δt
$[10^5 : 10^9]$	0.01	0.1	$[512 \times 512 : 1536 \times 1536]$	5×10^{-5}
$[3 \times 10^5 : 3 \times 10^8]$	0.01	0.1	$[512 \times 512 : 1280 \times 1280]$	5×10^{-5}
10^7	$[0.001 : 0.3]$	0.1	1024×1024	5×10^{-5}
10^7	0.01	$[0.02 : 2]$	1024×1024	5×10^{-5}

Table 1. List of the numerical simulations in this study.
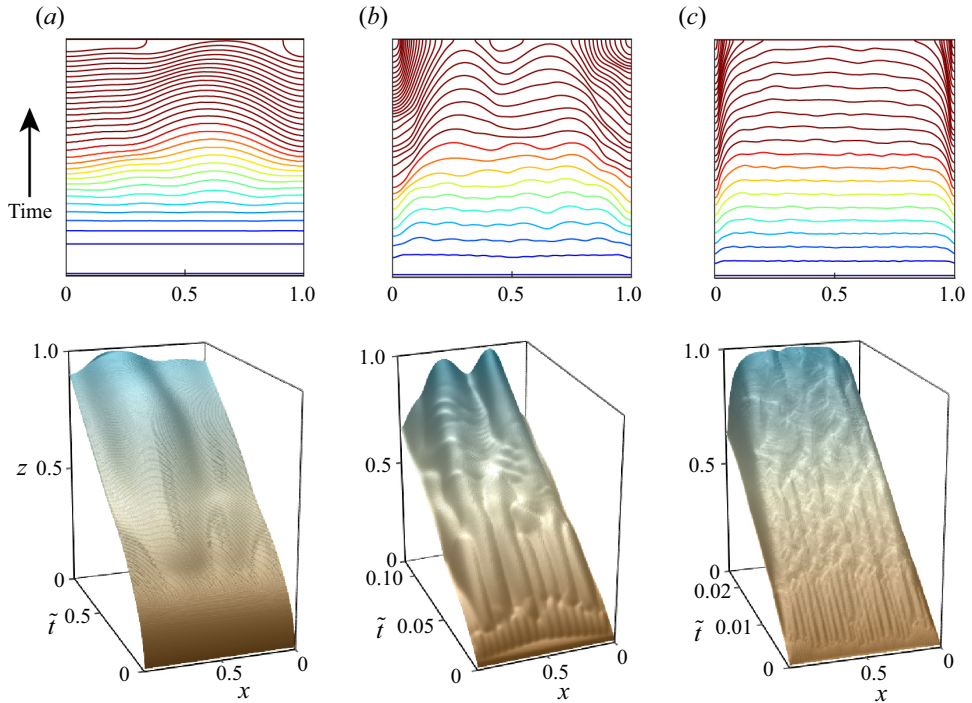
Figure 2. Temporal evolution of the liquid–solid interface for vibration-induced melting in microgravity for different vibrational Rayleigh numbers (*a*) $Ra_{vib} = 10^5$, (*b*) $Ra_{vib} = 10^7$ and (*c*) $Ra_{vib} = 10^9$ at fixed $Pr = 10$.

$\xi(x, t)$ is extracted at the interface location where the phase-field value is $\phi = 0.5$. It is observed that, initially, the interface is relatively uniform along the x direction, indicating that heat transfer is dominated by conduction. As $\xi(x, t)$ increases with time, vibration-induced convection becomes the primary mode of heat transfer, leading to increased roughness of the interface.

We then examine the evolution of the mean interface height $\bar{\xi}(t) = \langle \xi(x, t) \rangle_x$ during vibration-induced melting, where $\langle \cdot \rangle_x$ denotes the average over a specific horizontal plane. Figure 3(*a*) shows the measured mean height $\bar{\xi}(t)$ as a function of $\tilde{t}$ for different Ra_{vib}, where $\tilde{t} = t\sqrt{Pr/(2Ra_{vib})}$ denotes the time scaled by the viscous time scale. It is seen that the trend of $\bar{\xi}(t)$ exhibits two distinct scaling laws with time $\tilde{t}$, i.e. $\bar{\xi} \sim \tilde{t}^{1/2}$ during the early evolution and $\bar{\xi} \sim \tilde{t}$ for the later time. We further plot the interface evolution rate $\dot{\bar{\xi}} = d\bar{\xi}/d\tilde{t}$ as a function of $\bar{\xi}$. Two different scaling laws are identified. At lower vibration Rayleigh numbers, $\dot{\bar{\xi}} \sim \bar{\xi}^{-1}$, while at higher vibration Rayleigh numbers, a flattening of
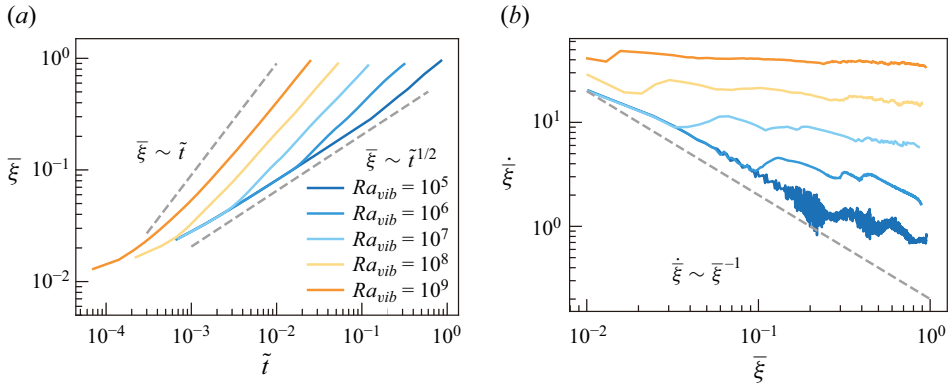
Figure 3. (*a*) The measured mean interface height $\bar{\xi}$ as a function of $\tilde{t}$ for different Ra_{vib}. (*b*) The measured interfacial evolution rate $\dot{\bar{\xi}}$ as a function of the mean interface height $\bar{\xi}$ for different Ra_{vib}. In (*a*), $\tilde{t}$ is the dimensionless time by a viscous time scale and the dashed lines represent $\bar{\xi} \sim \tilde{t}^{1/2}$ and $\bar{\xi} \sim \tilde{t}$. In (*b*), the dashed line represents $\dot{\bar{\xi}} \sim \bar{\xi}^{-1}$.

scaling occurs, characterized by $\dot{\bar{\xi}} \sim \bar{\xi}^0$, implying that the melting rate of the interface becomes constant, independent of the mean interface height and time.

As the melting is related to the heat transfer mechanism at the liquid–solid interface, we then try to explain those scaling relations from the relation between melting rate and the vertical heat flux. From the Stefan boundary condition (2.5), one obtains

$$\bar{\xi}\frac{\mathrm{d}\bar{\xi}}{\mathrm{d}t} = \frac{1}{St\sqrt{2Ra_{vib}Pr}}Nu_{eff}, \tag{3.1}$$

where the effective Nusselt number Nu_{eff} represents the ratio of the vertical heat flux at the liquid–solid interface to the diffusive flux across the liquid layer of a mean height $\bar{\xi}$. We calculate Nu_{eff} according to (3.1). Similar to the heat transport scaling relation in a microgravity vibroconvection system, one can assume that the effective Nusselt number has power-law dependencies on vibrational Rayleigh number (Huang *et al.* 2024), i.e. $Nu_{eff} \sim Ra_{vib}^{eff\ \alpha}$ with $Ra_{vib}^{eff} = Ra_{vib}\bar{\xi}^2$. Substituting the Nu_{eff} relation into (3.1) allows us to obtain

$$\bar{\xi} \sim Ra_{vib}^{\alpha/(2-2\alpha)}Pr^{-(1/(2-2\alpha))}St^{-(1/(2-2\alpha))}\tilde{t}^{1/(2-2\alpha)}. \tag{3.2}$$

To quantify the value of the unknown α in $\bar{\xi}$-scaling relation (3.2), we plot in figure 4 the effective outgoing Nusselt number Nu_{eff} as a function of Ra_{vib}^{eff} for different Ra_{vib}. It is seen that Nu_{eff} is nearly constant for small Ra_{vib}, indicating $\alpha = 0$ in the conductive regime, while a scaling relation $Nu_{eff} \sim (Ra_{vib}^{eff})^{1/2}$ is obviously found for large Ra_{vib}, indicating $\alpha = 1/2$ in the convective regime (Huang *et al.* 2024). Substituting $\alpha = 0$ and $\alpha = 1/2$ into (3.2) gives two known scaling behaviours of melting rate which are identified above: $\bar{\xi} \sim \tilde{t}^{1/2}$ and $\bar{\xi} \sim \tilde{t}$. This well explains the transition from $\bar{\xi} \sim \tilde{t}^{1/2}$ in the conductive regime to $\bar{\xi} \sim \tilde{t}$ in the vibration-induced convection regime. It is worth noting that when a larger amplitude a is used, the system's heat transfer characteristics need to be described by the oscillatory Rayleigh number $Ra_{os} = (\beta A\Omega^2\Delta H^3)/vk$ (Huang *et al.* 2024). However, this does not affect the scaling law between $\bar{\xi}$ and $\tilde{t}$. This transition of melting rate from diffusive to convective regimes is also found in solid melting driven by Rayleigh–Bénard convection (Favier *et al.* 2019).
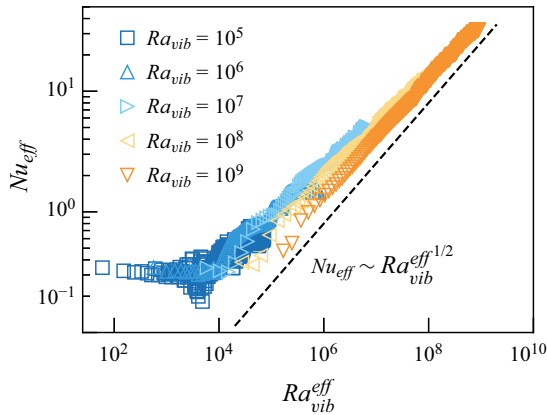
Figure 4. The measured interfacial effective Nusselt number Nu_{eff} as a function of effective vibrational Rayleigh number Ra_{vib}^{eff} for different Ra_{vib}. The dashed line represents $Nu_{eff} \sim Ra_{vib}^{eff\,1/2}$.

4. Fluid layer dynamics and its influence on interface shape

Upon establishing a fundamental comprehension of the evolution of mean interface height, attention is redirected towards the underlying dynamics of vibroconvective flow in the liquid layer, which catalyses the genesis of intricate interface morphology. Figure 5 shows the instantaneous flow structure by visualizing the temperature field and velocity field at different mean height $\bar{\bar{\xi}}$ for vibrational Rayleigh numbers $Ra_{vib} = 10^5, 10^7, 10^9$. For a small vibrational Rayleigh number $Ra_{vib} = 10^5$ (see figure 5a) at $\bar{\bar{\xi}} = 0.2$, corresponding to $Ra_{vib}^{eff} = 4 \times 10^3$, the flow structure in the liquid layer exhibits a periodic circulation with a stable temperature distribution in the bulk region. With increasing $\bar{\bar{\xi}}$ (or the effective vibrational Rayleigh number Ra_{vib}^{eff}), the periodic circulation intensifies to disturb the temperature field, leading to a slight shift of heat transfer from the pure convection regime. For high vibrational Rayleigh numbers, e.g. $Ra_{vib} = 10^7$ and $Ra_{vib} = 10^9$ as shown in figure 5(b,c), since the vibration-induced shear effect becomes strong enough to destabilize the thermal boundary layer, massive columnar thermal plumes erupt from the thermal boundary layer and the flow structure transits into the columnar regime. We notice that as melting proceeds with time, vertical columnar plumes merge into larger and wider plumes. And due to adiabatic and no-slip boundary conditions at the sidewalls, the peripheral flow is formed and leads to heat accumulation near the sidewalls. Both phenomena of plume merging and heat accumulation in peripheral flow near the sidewall result in a more complicated morphology evolution of the liquid–solid interface.

We start to focus on the effect of plume merging on the morphology evolution of the liquid–solid interface. During the melting process, columnar plumes are generated due to the vibroconvective instability, and they gradually grow under vibration-induced buoyancy until reaching the saturation state. In presence of vertical stretching, new convective instability occurs and causes adjacent plumes to merge, resulting in the formation of larger and more stable columnar thermal structures. Figure 6 presents the temporal evolution of the temperature profile at mid-height $z = \bar{\bar{\xi}}/2$ of the liquid domain and clearly shows the merging behaviour of the thermal plumes during melting at $Ra_{vib} = 10^7$ and $Ra_{vib} = 10^9$, where the flow structure is almost in the columnar regime. It is seen that after the transition to the columnar regime, massive plumes begin to erupt abruptly, and gradually merge into
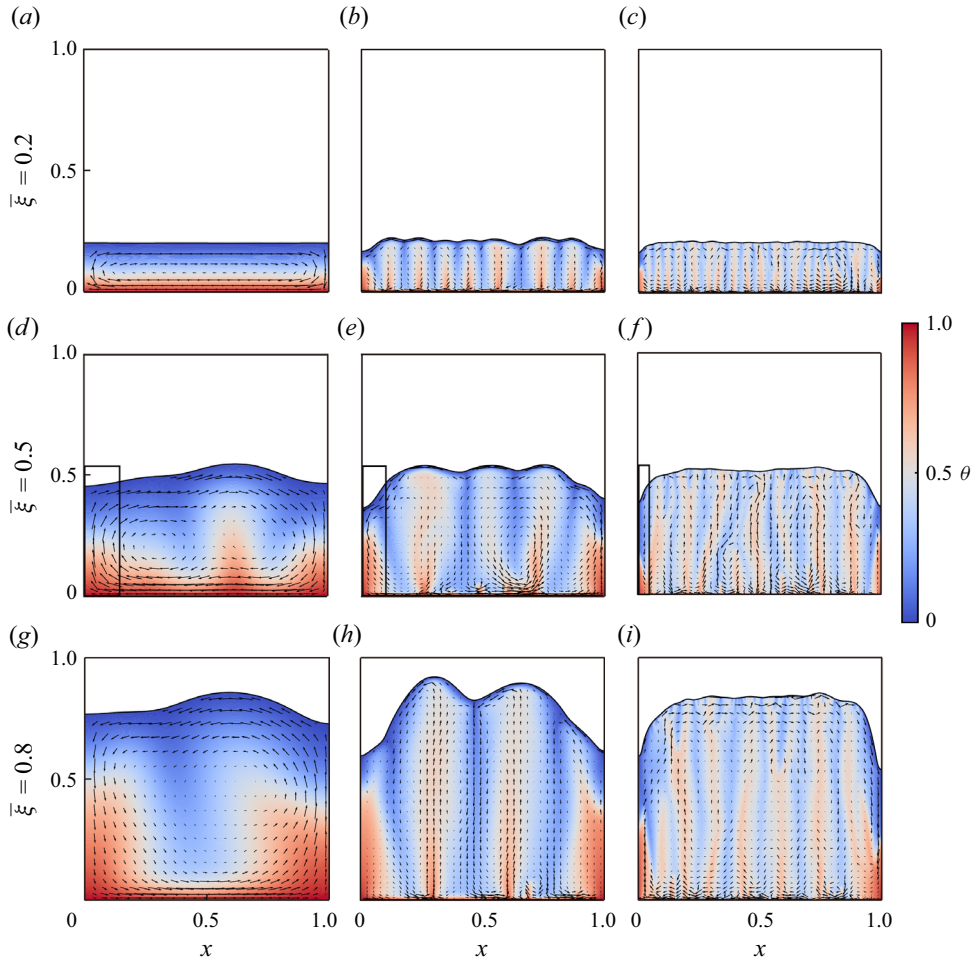
Figure 5. Instantaneous snapshots of the temperature (colour) and velocity (vectors) fields for three different $\bar{\bar{\xi}}$, which are (a–c) $\bar{\bar{\xi}} = 0.2$, (d–f) $\bar{\bar{\xi}} = 0.5$ and (g–i) $\bar{\bar{\xi}} = 0.8$, and for three different Ra_{vib}, which are (a,d,g) $Ra_{vib} = 10^5$, (b,e,h) $Ra_{vib} = 10^7$ and (c,f,i) $Ra_{vib} = 10^9$. The rectangles in (d–f) show the region of peripheral flow near the left sidewall.

larger and stable ones with $\bar{\bar{\xi}}$ (or Ra_{vib}^{eff}) further increasing. This phenomenon is similar to the merging of convective rolls observed in the melting process in Rayleigh–Bénard convection by Favier *et al.* (2019), where there is an alternation between stable solutions, chaotic solutions and ultimately a transition to turbulent solutions.

To quantitatively investigate the merging behaviour of columnar plumes, we plot the number of columnar thermal plumes K_m as a function of the mean interface height $\bar{\bar{\xi}}$ in figure 7(a). Here, K_m is obtained by counting the number of extreme points in the temperature profile at mid-height $z = \bar{\bar{\xi}}/2$ of the liquid domain, which is filtered by using $T - T_m > cT_{rms}$ to remove the small-scales noise with the tuning coefficient $c = 0.8$. In fact, when $0.6 \leq c \leq 1.0$, the obtained results are not sensitive to the choice of c. It is observed that with increasing $\bar{\bar{\xi}}$, the number of columnar plumes initially increases, which corresponds to the transition of flow structure from the periodic-circulation regime to the columnar regime, then reaches a maximum and gradually decreases due to the alternating
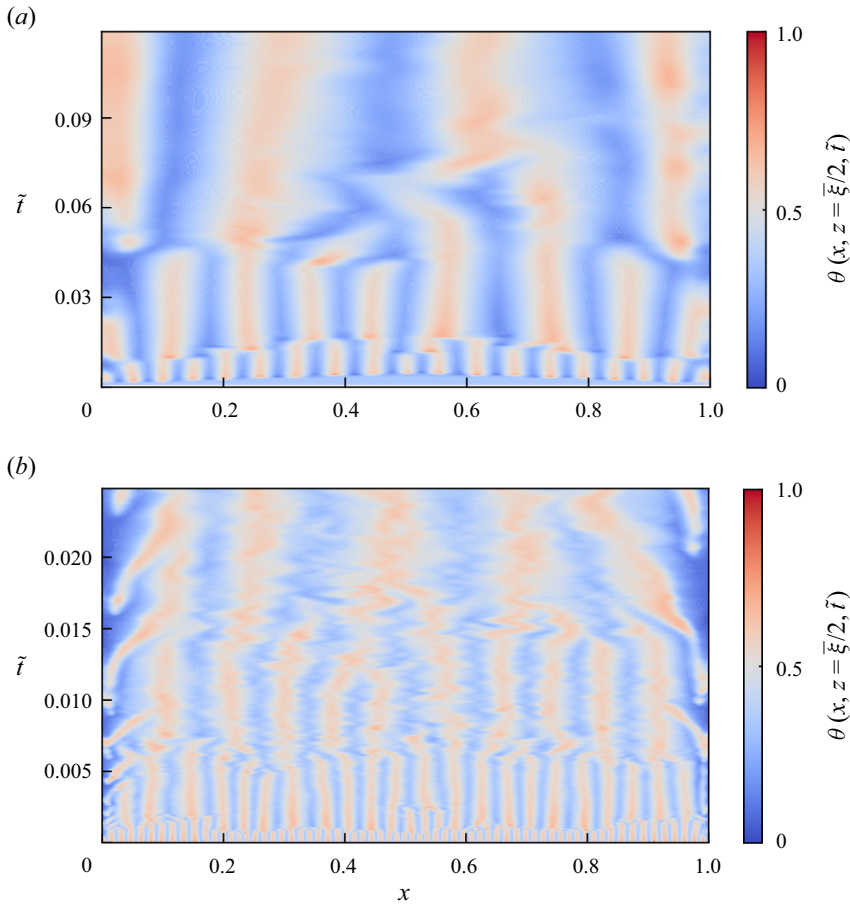
(*a*)

(*b*)

Figure 6. Spatio-temporal evolution of the temperature profile at the mid-height of the liquid domain for two vibrational Rayleigh numbers (*a*) $Ra_{vib} = 10^7$ and (*b*) $Ra_{vib} = 10^9$.

occurrence of secondary bifurcation and nonlinear saturation (Favier *et al.* 2019). Due to the oscillatory behaviour of vibroconvective flows, the profiles of K_m exhibit some oscillations. By fitting with these profiles in the columnar regime, we found that for the plume merging behaviour, there exists a scaling relation between the columnar plume number K_m and the mean interface height $\bar{\xi}$, i.e. $K_m \sim \bar{\xi}^{-0.70\pm0.05}$.

How can we understand the obtained scaling relation of the columnar plume merging behaviour? We find that the underlying mechanism of plume merging consists of two aspects: one is the effect of the aspect ratio of the liquid layer quantified by the ratio of height to width Γ, and the other is the effect of vibrational intensity quantified by the parameter Ra_{vib}. For the effect of aspect ratio Γ, as the number of columnar plumes linearly increases with increasing width of the liquid layer at fixed height, there exists an inverse relationship between K_m and aspect ratio Γ, i.e. $K_m \sim \Gamma^{-1}$. For the Ra_{vib} effect, we assume that the columnar plume number K_m has a power-law dependency on the vibrational Rayleigh number, i.e. $K_m \sim Ra_{vib}^{\gamma}$ with γ the scaling exponent. During the vibration-induced melting process, both effects contribute to the plume merging behaviour, leading to the scaling relation of K_m between the aspect ratio $\Gamma = \bar{\xi}$ and the
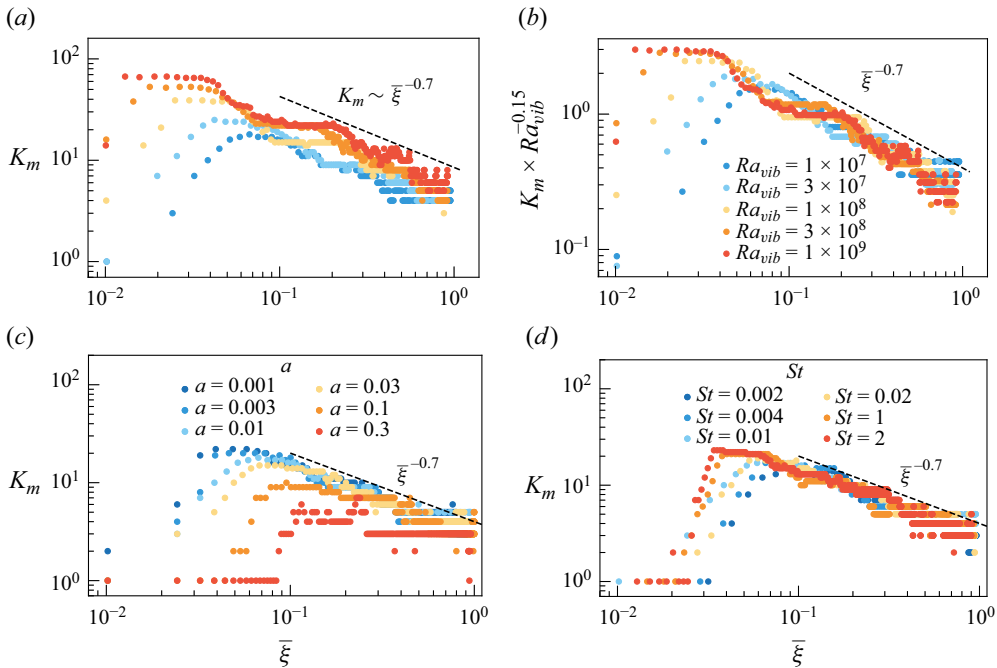
1001 A43-10

Figure 7. The number of columnar thermal plumes (*a*) K_m and its rescaled quantity (*b*) $K_m Ra_{vib}^{-0.15}$ as functions of the mean interface height $\bar{\xi}$ for different Ra_{vib}, which are $Ra_{vib} = 1 \times 10^7$, 3×10^7, 1×10^8, 3×10^8 and 1×10^9. Plots of K_m as a function of $\bar{\xi}$ for different (*c*) *a* and (*d*) *St*, with $Ra_{vib} = 10^7$. The dashed lines in (*a–d*) represent the scaling relation of $\bar{\xi}^{-0.7}$. The symbols represent the results calculated based on the statistical criteria for columnar thermal plumes.

effective Rayleigh number Ra_{vib}^{eff} of the instantaneous liquid layer, i.e. $K_m \sim \bar{\xi}^{-1}(Ra_{vib}^{eff})^{\gamma}$. Applying $Ra_{vib}^{eff} = Ra_{vib}\bar{\xi}^2$ allows one to rewrite the above relationship: $K_m \sim Ra_{vib}^{\gamma}\bar{\xi}^{2\gamma-1}$. Using the obtained scaling relation $K_m \sim \bar{\xi}^{-0.70\pm0.05}$ in figure 7(*a*), one readily obtains $\gamma = 0.150 \pm 0.025$. The error mainly comes from the varying durations of nonlinear saturation phases for different Ra_{vib} and minor inaccuracies in counting plume columns. To further confirm the deduced relationship $K_m \sim Ra_{vib}^{\gamma}\bar{\xi}^{2\gamma-1}$ with $\gamma = 0.150 \pm 0.025$, we replot figure 7(*a*) by showing $K_m Ra_{vib}^{-0.15}$ as a function of $\bar{\xi}$ in figure 7(*b*). It is found that the curves in the stage of plume merging for all Ra_{vib} studied almost collapse showing a remarkable scaling relation: $\bar{\xi}^{-0.7}$. Additionally, it is noteworthy that the value of K_m is influenced by factors such as *St*, *a* and initial perturbations. Particularly in figure 7(*c*), it can be observed that when Ra_{vib} remains constant, the value of K_m decreases significantly with an increase of *a*. This change is related to the transition in the heat transport mechanism of vibroconvective turbulence (Huang *et al.* 2024). However, as depicted in figure 7(*c,d*), for various *St* and smaller values of *a*, the merging behaviour of columnar plumes is invariant. Specifically, for a substantial value of *a*, such as $a = 0.3$, the number of plumes is significantly reduced, rendering the merging pattern less discernible.

We then examine the effect of peripheral flow near sidewalls on the morphology evolution of the liquid–solid interface. Figure 8 shows cumulative basal melting rates $(\bar{\xi} - 0.01)/\tilde{t}_{\bar{\xi}}$ at different mean interface heights for different Ra_{vib}. It is seen that the melting rate near sidewalls is obviously lower than that in the central region, indicating that the melting mechanism by peripheral flow is different from that by the upward
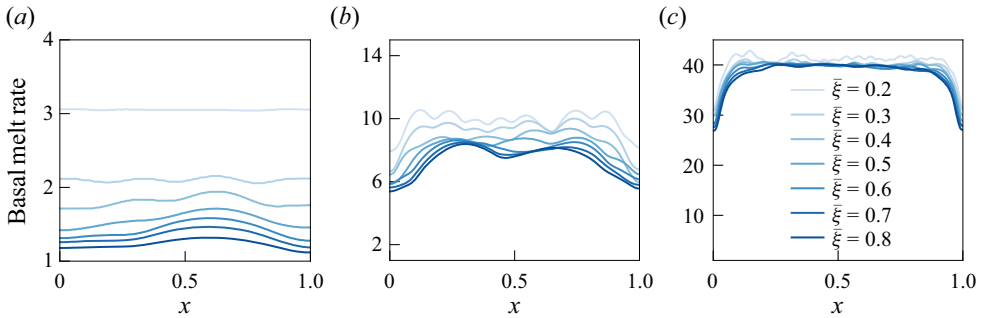
Figure 8. The cumulative basal melt rate at various mean interface heights $\bar{\bar{\xi}}$ for different vibrational Rayleigh numbers (a) $Ra_{vib} = 10^5$, (b) $Ra_{vib} = 10^7$ and (c) $Ra_{vib} = 10^9$.

and downward columnar plumes. To illustrate the flow characteristics of the peripheral flow region, we plot five snapshots of the instantaneous temperature and velocity fields within one vibration period for $Ra_{vib} = 10^7$ in figure 9(a–e). We observe that during the upper half of the vibration period, the outer flow region exhibits an upward flow trend, while in the lower half of the period, the trend is reversed. Additionally, we plot the time evolution of vertical velocity profiles over $0 \le x \le 0.1$ and $z = 0.1$ over three dimensionless time periods, normalized by the vibration period $\tau_w = 2\pi a$, as shown in figure 9(f). It is evident that the vertical velocity exhibits periodic variations, with a period matching the applied harmonic vibration period. We analyse the effect of peripheral flow only in near-sidewall regions for $0 \le x < 1/3$ and $2/3 < x \le 1$, to minimize the influence of columnar plumes in central regions. We define the mean interface height shift $\xi_s(t) = (\xi_{s,left}(t) + \xi_{s,right}(t))/2$ from the sidewalls to the central regions, where the height shifts for left and right sidewalls are given by

$$\xi_{s,left}(t) = \max\{\xi(x,t)\} - \min\{\xi(x,t)\} \quad \text{for } 0 \le x < 1/3, \tag{4.1}$$

$$\xi_{s,right}(t) = \max\{\xi(x,t)\} - \min\{\xi(x,t)\} \quad \text{for } 2/3 < x \le 1. \tag{4.2}$$

Figure 10 shows the temporal evolution of $\xi_s(t)$ for different Ra_{vib}. One sees that the interface height shift $\xi_s(t)$ vanishes in the diffusive regime, whereas $\xi_s(t)$ grows with time due to the presence of peripheral flow in vibration-induced convection regime. Additionally, with increasing Ra_{vib}, the maximum value of $\xi_s(t)$ initially rises, indicating a greater difference in local heat flux between the columnar thermal structure and peripheral flow regions. At higher Ra_{vib}, the melting of the upper interface in the peripheral flow region is likely to be disrupted by nearby thermal plumes, as more thermal plumes are generated, reducing the size of the peripheral flow region. In this case, $\xi_s(t)$ may decrease. Finally, it should be emphasized that in a thermal vibrational convection system bounded laterally by walls, heat tends to accumulate near the sidewalls (Guo *et al.* 2023). When phase change is involved, these wall patterns lead to a reduced melting rate near the sidewalls. It is worth noting that in a rotating system bounded by lateral walls, Ravichandran & Wettlaufer (2021) found that heat is primarily transferred through peripheral flow, and the melting rate of the solid region near the wall is significantly faster than that of the interior. This is different from our conclusions, suggesting that the influence of peripheral flow may vary across different systems.
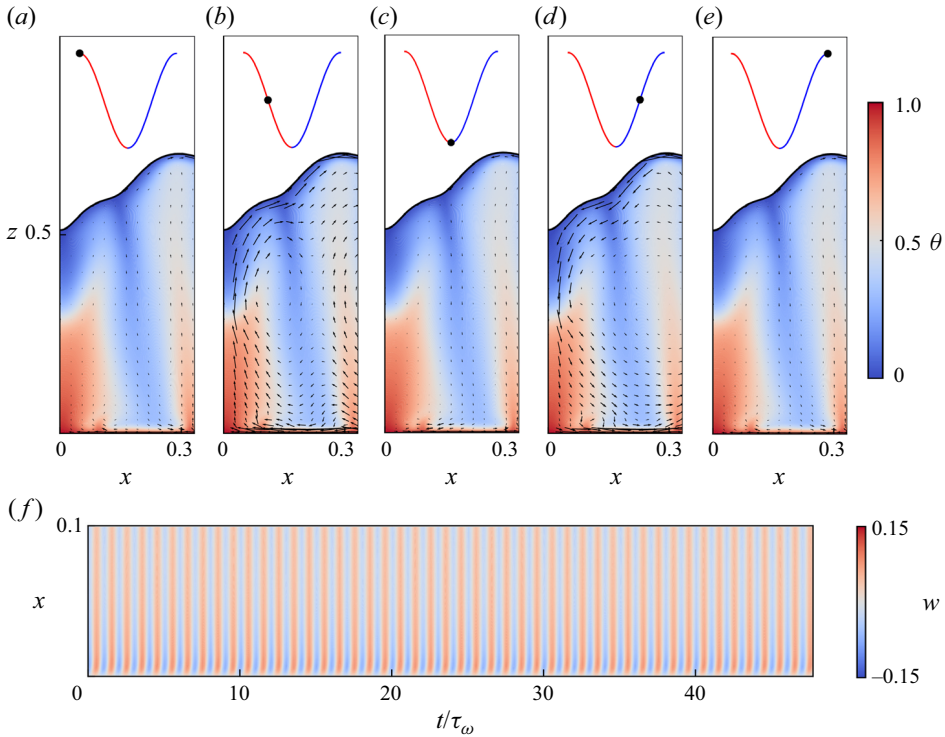
Figure 9. Instantaneous temperature and velocity fields for $Ra_{vib} = 10^7$ at phases (*a*) 0, (*b*) $\pi/2$, (*c*) π, (*d*) $3\pi/2$ and (*e*) 2π. (*f*) Time evolution of the vertical velocity $T|_{0 \leq x \leq 0.1, z=0.1}$. The black circles in the insets of (*a–e*) indicate the corresponding instant of the phase.
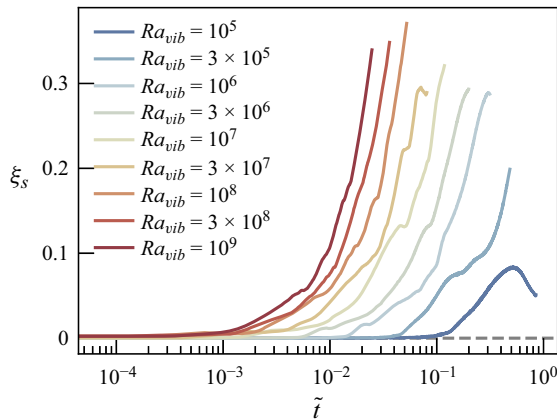

Figure 10. The measured mean interface height shift ξ_s during the process from the beginning to the interface touching the top plate.

5. Interface roughness characteristics

As both the plume merging and the peripheral flow near sidewalls affect the evolution of intricate interface patterns, it raises a question as to how the roughness of the interface evolves with time. The characteristics of interface roughness are quantified by the root
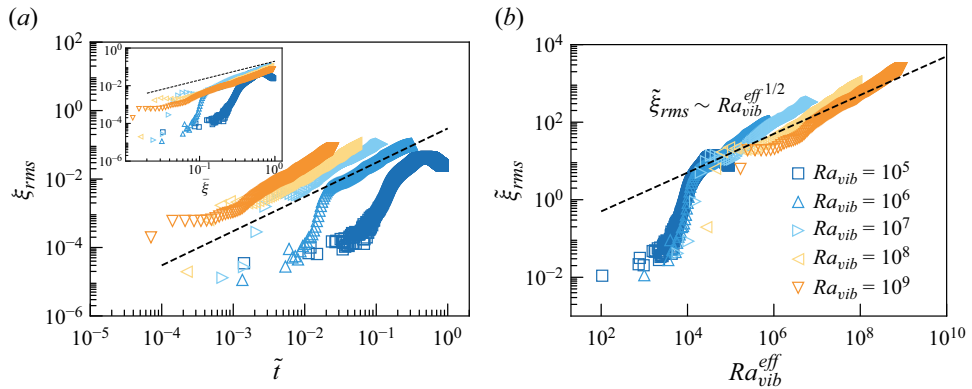
Figure 11. (*a*) The measured interface roughness amplitude ξ_{rms} as a function of $\tilde{t}$. The inset further shows ξ_{rms} as a function of mean interface height $\bar{\xi}$. (*b*) Rescaled roughness amplitude $\tilde{\xi}_{rms}$ as a function of vibrational Rayleigh number Ra_{vib}^{eff}. The dashed line in (*a*) represents $\xi_{rms} \sim \tilde{t}$ and the dashed line in the inset of (*a*) represents $\xi_{rms} \sim \bar{\xi}$. The dashed line in (*b*) represents $\tilde{\xi}_{rms} \sim Ra_{vib}^{eff\,1/2}$.

mean square (r.m.s.) of the interface height fluctuation, $\xi_{rms} = \sqrt{\overline{\xi'^2}}$ with $\xi' = \xi - \bar{\xi}$ the interface height fluctuation. Figure 11(*a*) plots the measured ξ_{rms} as a function of time for different Ra_{vib}. It is shown that after the transition to the columnar regime, ξ_{rms} seems to linearly grow with time, i.e. $\xi_{rms} \sim \tilde{t}$. As the mean height obeys $\bar{\xi} \sim \tilde{t}$ in the columnar regime from (3.2), it allows one to obtain the relation between ξ_{rms} and $\bar{\xi}$, namely $\xi_{rms} \sim \bar{\xi}$, indicating that the r.m.s. height is proportional to the mean height as shown in the inset of figure 11(*a*). By rescaling ξ_{rms} as $\tilde{\xi}_{rms} = \xi_{rms} Ra_{vib}^{1/2}$, one can observe an approximate scaling law of $\tilde{\xi}_{rms} \sim Ra_{vib}^{eff\,1/2}$ as shown in figure 11(*b*). In addition, we investigate the influence of the amplitude *a* and Stefan number *St* on the scaling relation $\tilde{\xi}_{rms} \sim Ra_{vib}^{eff\,1/2}$. Figure 12 depicts $\tilde{\xi}_{rms}$ as a function of Ra_{vib}^{eff} for different amplitude *a* and Stefan number *St* at fixed Ra_{vib}. It is observed that the scaling relationship $\tilde{\xi}_{rms} \sim Ra_{vib}^{eff\,1/2}$ is quite robust, showing an independency on both the vibration amplitude and Stefan number.

To gain insight into this robust scaling law $\tilde{\xi}_{rms} \sim Ra_{vib}^{eff\,1/2}$, we follow an approach used in buoyancy-driven melting in Rayleigh–Bénard convection by Yang *et al.* (2023*b*), and try to theoretically understand it. We start from the Stefan boundary condition (2.5), which gives

$$\bar{\xi}\frac{\mathrm{d}\tilde{\xi}}{\mathrm{d}t} = \frac{\sqrt{2}}{2} St^{-1} Pr^{-1/2} Nu_{loc}, \tag{5.1}$$

where $\tilde{\xi} = Ra_{vib}^{1/2}\xi$, and the local Nusselt number Nu_{loc} represents the ratio of the vertical local heat flux at the liquid–solid interface to the diffusive flux across the liquid layer of a mean height $\bar{\xi}$. Subtracting (3.1) from (5.1), we obtain

$$\bar{\xi}\frac{\mathrm{d}\tilde{\xi}'}{\mathrm{d}t} = \frac{\sqrt{2}}{2} St^{-1} Pr^{-1/2} Nu'_{loc}, \tag{5.2}$$

where $\tilde{\xi}' = Ra_{vib}^{1/2}\xi'$, and $Nu'_{loc} = Nu_{loc} - Nu_{eff}$ is the fluctuating vertical local heat flux. By employing the chain rule, we can establish a connection between $\tilde{\xi}'$ and Ra_{vib}^{eff}, i.e.
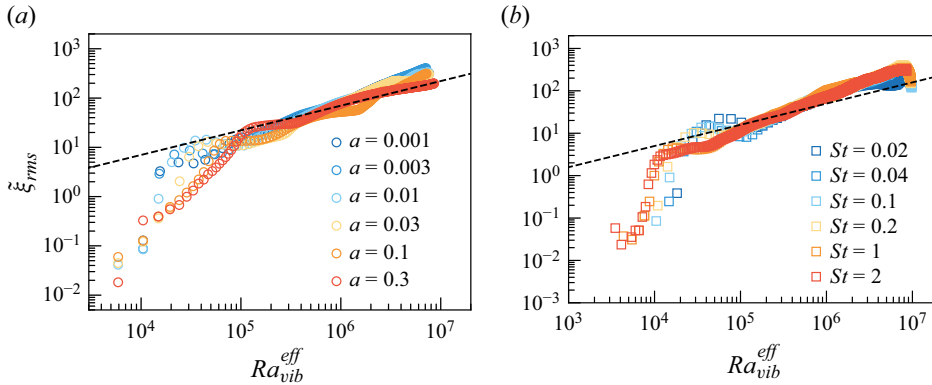
1001 A43-14

Figure 12. Rescaled interface roughness amplitude $\tilde{\xi}_{rms}$ as functions of vibrational Rayleigh number Ra_{vib}^{eff} (*a*) for different dimensionless vibration amplitude *a* and (*b*) for different *St*. The dashed lines in (*a*,*b*) represent $\tilde{\xi}_{rms} \sim Ra_{vib}^{eff\,1/2}$.

$\partial \tilde{\xi}'/\partial Ra_{vib}^{eff} = (\partial \tilde{\xi}'/\partial t)(\partial t/\partial \bar{\xi})(\partial \bar{\xi}/\partial Ra_{vib}^{eff})$. Substituting (3.1) and (5.2) into the above equation of $\partial \tilde{\xi}'/\partial Ra_{vib}^{eff}$, one obtains

$$\frac{\partial \tilde{\xi}'}{\partial Ra_{vib}^{eff}} = \frac{Nu'_{loc}}{2Nu_{eff}}Ra_{vib}^{eff\,-1/2}. \tag{5.3}$$

Equation (5.3) shows the relation between ξ' and Ra_{vib}^{eff} with the unknown term Nu'_{loc}/Nu_{eff}. Here, we measure the conditionally averaged heat fluxes for the hot and cold regions and plot the normalized heat flux fluctuations as a function of Ra_{vib}^{eff} for different control parameters Ra_{vib}, *St* and *a* in figure 13. It can be observed that within a wide range from $Ra_{vib}^{eff} = 10^5$ to $Ra_{vib}^{eff} = 10^9$, the contributions to the heat flux from the hot and cold regions remain nearly constant. Since Nu'_{loc}/Nu_{eff} can be estimated from the difference in the averaged heat flux between the hot and cold regions, one can approximate $Nu'_{loc}/Nu_{eff} \sim$ constant, namely $Nu'_{loc}/Nu_{eff} \approx R_{Nu}$, and integrating (5.3) over Ra_{vib}^{eff} allows one to obtain $\tilde{\xi}' \approx R_{Nu}Ra_{vib}^{eff\,1/2}$. Substituting $\tilde{\xi}' \approx R_{Nu}Ra_{vib}^{eff\,1/2}$ into $\tilde{\xi}_{rms} = \sqrt{\overline{\tilde{\xi}'^2}}$ leads to an analytical relation between $\tilde{\xi}_{rms}$ and Ra_{vib}^{eff}:

$$\tilde{\xi}_{rms} \sim Ra_{vib}^{eff\,1/2}, \tag{5.4}$$

which agrees well with the results in figures 11(*b*) and 12.

6. Concluding remarks and outlook

This study employs direct numerical simulation coupled with the phase-field method to study the melting process of a solid phase under two-dimensional vibroconvective flow in microgravity. It is shown that as melting progresses, the heat transfer mechanism transitions from thermal conduction to a vibration-driven thermal convection regime. Correspondingly, the flow structure evolves from a periodic-circulation regime to a columnar regime. The subtle flow structure leads to hot and cold regions in the liquid layer, resulting in non-uniform heat flux and causing the interface to become rough.
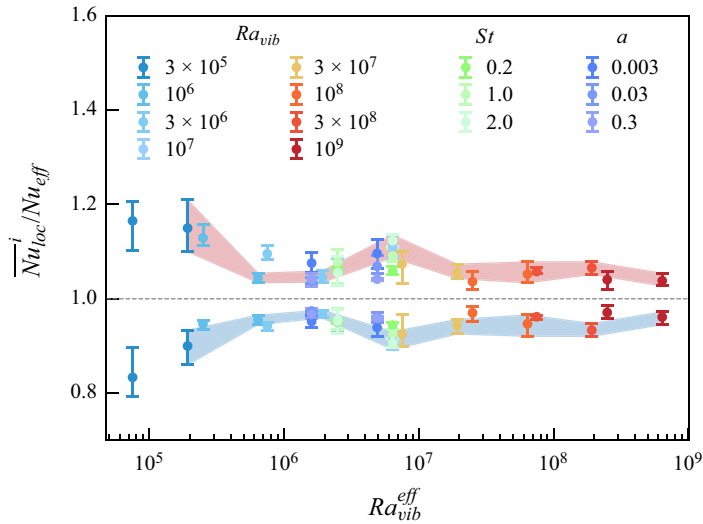
Figure 13. The conditionally vertical averaged heat fluxes in the hot region $\overline{Nu}_{loc}^{h}$ and cold region $\overline{Nu}_{loc}^{c}$, normalized by the vertical interface-averaged heat flux Nu_{eff}, as a function of effective vibrational Rayleigh number Ra_{vib}^{eff} for different Ra_{vib} and a at $\bar{\bar{\xi}} = 0.5$ and $\bar{\bar{\xi}} = 0.8$, and for different St at $\bar{\bar{\xi}} = 0.4$ and $\bar{\bar{\xi}} = 0.7$. The data points are calculated by taking the average over five consecutive time steps for each $\bar{\bar{\xi}}$, with error bars indicating the range of values.

We characterize the evolution of the liquid–solid interface morphology and find that the transition in the heat transfer mechanism leads to a power-law change in the dependency of the mean interface height on time. We also derive these scaling relations from the Stefan boundary condition based on the mean vertical heat flux at the interface, i.e. $\bar{\bar{\xi}} \sim \tilde{\imath}^{1/(2-2\alpha)}$, where the scaling exponent $\alpha = 0$ in the conductive regime and $\alpha = 1/2$ in the vibration-induced convective regime.

Furthermore, we find that the morphology evolution of the liquid–solid interface is mainly affected by both the merging behaviour of columnar thermal plumes and the peripheral flow near the sidewalls. This is controlled by the effects of the aspect ratio and vibrational intensity of the liquid layer, i.e. $K_m \sim \bar{\bar{\xi}}^{-1}(Ra_{vib}^{eff})^{\gamma}$, where K_m is the number of columnar plumes. Exponent $\gamma = 0.150 \pm 0.025$ is the fitting scaling exponent from numerical data, which is insensitive to the choice of St and a. We then examined the flow characteristics of the peripheral flow and conducted a statistical analysis of the mean interface height shift. Finally, we quantify the evolution characteristics of the interface roughness amplitude and find a power-law dependency of the normalized roughness amplitude on the effective vibrational Rayleigh number, $\tilde{\xi}_{rms} \sim Ra_{vib}^{eff\ 1/2}$. This scaling relation is found to be robust, showing independence from both the vibration amplitude and Stefan number. Starting from the Stefan boundary condition, we provide a theoretical derivation and demonstrate that this robust power-law relationship holds under the condition that the ratio of the fluctuating local heat flux to the total heat flux at the interface remains nearly constant.

Our findings provide a comprehensive understanding of the morphological changes of a melting solid under the influence of vibroconvection in microgravity. Vibration-induced melting in microgravity opens up new possibilities for actively controlling the melting processes of PCMs, with potential applications in microscale devices and devices for

future space exploration. It is worth noting that the vibration source may result in additional energy consumption, so it is important to focus on improving energy efficiency and cost-effectiveness during application. Future studies may consider exploring higher Ra_{vib}, where previous research on vibroconvection in single-phase systems reveals the emergence of gyroscopic structures at higher Ra_{vib} (Guo *et al.* 2023). This transition to large-scale flow structures is likely to significantly affect the melting process.

Declaration of interests. The authors report no conflict of interest.

Author ORCIDs.

Ⓘ Jian-Zhao Wu https://orcid.org/0000-0002-7981-3623;

Ⓘ Bo-Fu Wang https://orcid.org/0000-0001-6488-6275;

Ⓘ Quan Zhou https://orcid.org/0000-0002-0411-7228;

Ⓘ Kai Leong Chong https://orcid.org/0000-0002-3182-3689.

REFERENCES

BANNISTER, T., GRODZKA, P., SPRADLEY, L., BOURGEOIS, S., JR., HEDDEN, R. & FACEMIRE, B. 1973 Apollo 17 heat flow and convection experiments: final data analyses results. *NASA TM* X–64772.

BEYSENS, D. 2006 Vibrations in space as an artificial gravity? *Europhys. News* **37** (3), 22–25.

BRAIBANTI, M., *et al.* 2019 European space agency experiments on thermodiffusion of fluid mixtures in space. *Eur. Phys. J.* E **42**, 1–11.

BUSHUK, M., HOLLAND, D.M., STANTON, T.P., STERN, A. & GRAY, C. 2019 Ice scallops: a laboratory investigation of the ice–water interface. *J. Fluid Mech.* **873**, 942–976.

CARBO, R.M., SMITH, R.W. & POESE, M.E. 2014 A computational model for the dynamic stabilization of Rayleigh–Bénard convection in a cubic cavity. *J. Acoust. Soc. Am.* **135** (2), 654–668.

CHEN, X., HAO, G., YAO, F. & ZHANG, C. 2019 Numerical study on melting phase change under microgravity. *Microgravity Sci. Technol.* **31**, 793–803.

CHONG, K.L., QIAO, S., WU, J.-Z. & WANG, B.-F. 2024 Heat transfer enhancement in vertical convection under spatially harmonic temperature modulation. *Intl J. Heat Mass Transfer* **227**, 125452.

CISSÉ, I., BARDAN, G. & MOJTABI, A. 2004 Rayleigh–Bénard convective instability of a fluid under high-frequency vibration. *Intl J. Heat Mass Transfer* **47** (19-20), 4101–4112.

COUSTON, L.-A., HESTER, E., FAVIER, B., TAYLOR, J.R., HOLLAND, P.R. & JENKINS, A. 2021 Topography generation by melting and freezing in a turbulent shear flow. *J. Fluid Mech.* **911**, A44.

DAVIS, S.H., MÜLLER, U. & DIETSCHE, C. 1984 Pattern selection in single-component systems coupling Bénard convection and solidification. *J. Fluid Mech.* **144**, 133–151.

DEMIN, V., GERSHUNI, G. & VERKHOLANTSEV, I. 1996 Mechanical quasi-equilibrium and thermovibrational convective instability in an inclined fluid layer. *Intl J. Heat Mass Transfer* **39** (9), 1979–1991.

DHAIDAN, N.S., KHODADADI, J., AL-HATTAB, T.A. & AL-MASHAT, S.M. 2013 Experimental and numerical investigation of melting of NePCM inside an annular container under a constant heat flux including the effect of eccentricity. *Intl J. Heat Mass Transfer* **67**, 455–468.

DU, Y., WANG, Z., JIANG, L., CALZAVARINI, E. & SUN, C. 2023 Sea water freezing modes in a natural convection system. *J. Fluid Mech.* **960**, A35.

FAVIER, B., PURSEED, J. & DUCHEMIN, L. 2019 Rayleigh–Bénard convection with a melting boundary. *J. Fluid Mech.* **858**, 437–473.

FITZMAURICE, A., CENEDESE, C. & STRANEO, F. 2017 Nonlinear response of iceberg side melting to ocean currents. *Geophys. Res. Lett.* **44** (11), 5637–5644.

GARRABOS, Y., BEYSENS, D., LECOUTRE, C., DEJOAN, A., POLEZHAEV, V. & EMELIANOV, V. 2007 Thermoconvectional phenomena induced by vibrations in supercritical S F 6 under weightlessness. *Phys. Rev.* E **75** (5), 056317.

GERSHUNI, G.Z. & LYUBIMOV, D.V. 1998 *Thermal Vibrational Convection*. Wiley & Sons.

GLICKSMAN, M., LUPULESCU, A. & KOSS, M. 2003 Melting in microgravity. *J. Thermophys. Heat Transfer* **17** (1), 69–76.

GRODZKA, P.G. & BANNISTER, T.C. 1975 Heat flow and convection experiments aboard apollo 17. *Science* **187** (4172), 165–167.

GUO, C., QU, T., YU, Y. & ZHOU, J. 2024*a* Effects of mechanical vibration on melting characteristics of latent thermal energy storage units using the dynamic mesh method. *Appl. Therm. Engng* **252**, 123678.

GUO, X., QIN, P., WU, J., WANG, B., CHONG, K.L. & ZHOU, Q. 2024*b* Statistics of kinetic and thermal energy dissipation rates in two-dimensional thermal vibrational convection. *Phys. Fluids* **36** (7), 075132.

GUO, X.-L., WU, J.-Z., WANG, B.-F., ZHOU, Q. & CHONG, K.L. 2023 Flow structure transition in thermal vibrational convection. *J. Fluid Mech.* **974**, A29.

GUO, X.-Q., WANG, B.-F., WU, J.-Z., CHONG, K.L. & ZHOU, Q. 2022 Turbulent vertical convection under vertical vibration. *Phys. Fluids* **34** (5), 055106.

HESTER, E.W., COUSTON, L. -A., FAVIER, B., BURNS, K.J. & VASIL, G.M. 2020 Improved phase-field models of melting and dissolution in multi-component flows. *Proc. R. Soc.* A **476** (2242), 20200508.

HESTER, E.W., MCCONNOCHIE, C.D., CENEDESE, C., COUSTON, L.-A. & VASIL, G. 2021 Aspect ratio affects iceberg melting. *Phys. Rev. Fluids* **6** (2), 023802.

HOCK, R. 2005 Glacier melt: a review of processes and their modelling. *Prog. Phys. Geog.* **29** (3), 362–391.

HOSSEINIZADEH, S., DARZI, A.R. & TAN, F. 2012 Numerical investigations of unconstrained melting of nano-enhanced phase change material (NEPCM) inside a spherical container. *Intl J. Therm. Sci.* **51**, 77–83.

HUANG, Z.-L., GUO, X.-L., WU, J.-Z., WANG, B.-F., CHONG, K.L. & ZHOU, Q. 2023 Rayleigh-number dependence of the critical vibration frequency in vibrating thermal turbulence. *Phys. Rev. Fluids* **8** (11), 113501.

HUANG, Z.-L., WU, J.-Z., GUO, X.-L., ZHAO, C.-B., WANG, B.-F., CHONG, K.L. & ZHOU, Q. 2024 Unifying constitutive law of vibroconvective turbulence in microgravity. *J. Fluid Mech.* **987**, A14.

KAMKARI, B. & AMLASHI, H.J. 2017 Numerical simulation and experimental verification of constrained melting of phase change material in inclined rectangular enclosures. *Intl Commun. Heat Mass Transfer* **88**, 211–219.

LI, X., MA, T., LIU, J., LIU, L. & WANG, Q. 2017 Investigation of gravity effect on phase change heat transfer using the Lattice Boltzmann method. *Energy Procedia* **142**, 3902–3907.

MAHMUD, H. & AHMED, D.H. 2022 Numerical investigations on melting of phase change material (PCM) with different arrangements of heat source-sink pairs under microgravity. *Microgravity Sci. Technol.* **34** (2), 20.

MENG, W.-S., ZHAO, C.-B., WU, J.-Z., WANG, B.-F., ZHOU, Q. & CHONG, K.L. 2024 Simulation of flow and debris migration in extreme ultraviolet source vessel. *Phys. Fluids* **36** (2), 023322.

MIALDUN, A., RYZHKOV, I., MELNIKOV, D. & SHEVTSOVA, V. 2008 Experimental evidence of thermal vibrational convection in a nonuniformly heated fluid in a reduced gravity environment. *Phys. Rev. Lett.* **101** (8), 084501.

PORTER, J., SÁNCHEZ, P.S., SHEVTSOVA, V. & YASNOU, V. 2021 A review of fluid instabilities and control strategies with applications in microgravity. *Math. Model. Nat. Pheno.* **16**, 24.

PURSEED, J., FAVIER, B., DUCHEMIN, L. & HESTER, E.W. 2020 Bistability in Rayleigh–Bénard convection with a melting boundary. *Phys. Rev. Fluids* **5** (2), 023501.

RAHMANIAN, S., RAHMANIAN-KOUSHKAKI, H., MOEIN-JAHROMI, M. & SAIDUR, R. 2023 A novel method to improve the performance of pcm thermal energy storage units using a small oscillator plate-numerical analysis. *J. Energy Storage* **73**, 108900.

RAOUX, S. 2009 Phase change materials. *Annu. Rev. Mater. Res.* **39**, 25–48.

RAVICHANDRAN, S. & WETTLAUFER, J.S. 2021 Melting driven by rotating Rayleigh–Bénard convection. *J. Fluid Mech.* **916**, A28.

SÁNCHEZ, P.S., EZQUERRO, J., FERNANDEZ, J. & RODRIGUEZ, J. 2020*a* Thermocapillary effects during the melting of phase change materials in microgravity: heat transport enhancement. *Intl J. Heat Mass Transfer* **163**, 120478.

SÁNCHEZ, P.S., EZQUERRO, J., FERNANDEZ, J. & RODRIGUEZ, J. 2021 Thermocapillary effects during the melting of phase-change materials in microgravity: steady and oscillatory flow regimes. *J. Fluid Mech.* **908**, A20.

SÁNCHEZ, P.S., GAPONENKO, Y., YASNOU, V., MIALDUN, A., PORTER, J. & SHEVTSOVA, V. 2020*b* Effect of initial interface orientation on patterns produced by vibrational forcing in microgravity. *J. Fluid Mech.* **884**, A38.

SÁNCHEZ, P.S., YASNOU, V., GAPONENKO, Y., MIALDUN, A., PORTER, J. & SHEVTSOVA, V. 2019 Interfacial phenomena in immiscible liquids subjected to vibrations in microgravity. *J. Fluid Mech.* **865**, 850–883.

Šeta, B., Dubert, D., Gavalda, J., Massons, J., Bou-Ali, M.M., Ruiz, X. & Shevtsova, V. 2023 Effect of heat transfer through an interface on convective melting dynamics of phase change materials. *J. Fluid Mech.* **966**, A46.

Shevtsova, V., Ryzhkov, I.I., Melnikov, D.E., Gaponenko, Y.A. & Mialdun, A. 2010 Experimental and theoretical study of vibration-induced thermal convection in low gravity. *J. Fluid Mech.* **648**, 53–82.

Thomas, S.K., Cassoni, R.P. & MacArthur, C.D. 1996 Aircraft anti-icing and de-icing techniques and modeling. *J. Aircraft* **33** (5), 841–854.

Ulvrová, M., Labrosse, S., Coltice, N., Råback, P. & Tackley, P. 2012 Numerical modelling of convection interacting with a melting and solidification front: application to the thermal evolution of the basal magma ocean. *Phys. Earth Planet. Inter.* **206**, 51–66.

Wang, B.-F., Zhou, Q. & Sun, C. 2020 Vibration-induced boundary-layer destabilization achieves massive heat-transport enhancement. *Sci. Adv.* **6** (21), eaaz8239.

Wang, Z., Calzavarini, E., Sun, C. & Toschi, F. 2021 How the growth of ice depends on the fluid dynamics underneath. *Proc. Natl Acad. Sci. USA* **118** (10), e2012870118.

Wilson, N.J., Vreugdenhil, C.A., Gayen, B. & Hester, E.W. 2023 Double-diffusive layer and meltwater plume effects on ice face scalloping in phase-change simulations. *Geophys. Res. Lett.* **50** (17), e2023GL104396.

Wu, J.-Z., Dong, Y.-H., Wang, B.-F. & Zhou, Q. 2021 Phase decomposition analysis on oscillatory Rayleigh–Bénard turbulence. *Phys. Fluids* **33** (4), 045108.

Wu, J.-Z., Wang, B.-F., Chong, K.L., Dong, Y.-H., Sun, C. & Zhou, Q. 2022*a* Vibration-induced 'anti-gravity' tames thermal turbulence at high Rayleigh numbers. *J. Fluid Mech.* **951**, A13.

Wu, J.-Z., Wang, B.-F. & Zhou, Q. 2022*b* Massive heat transfer enhancement of Rayleigh–Bénard turbulence over rough surfaces and under horizontal vibration. *Acta Mechanica Sin.* **38** (2), 321319.

Yang, R., Chong, K.L., Liu, H.-R., Verzicco, R. & Lohse, D. 2022 Abrupt transition from slow to fast melting of ice. *Phys. Rev. Fluids* **7** (8), 083503.

Yang, R., Howland, C.J., Liu, H.-R., Verzicco, R. & Lohse, D. 2023*a* Ice melting in salty water: layering and non-monotonic dependence on the mean salinity. *J. Fluid Mech.* **969**, R2.

Yang, R., Howland, C.J., Liu, H.-R., Verzicco, R. & Lohse, D. 2023*b* Morphology evolution of a melting solid layer above its melt heated from below. *J. Fluid Mech.* **956**, A23.

Yang, R., Howland, C.J., Liu, H.-R., Verzicco, R. & Lohse, D. 2024 Shape effect on solid melting in flowing liquid. *J. Fluid Mech.* **980**, R1.

Zhang, Y. & Zhou, Q. 2024 Low-Prandtl-number effects on global and local statistics in two-dimensional Rayleigh–Bénard convection. *Phys. Fluids* **36** (1), 015107.

Zhao, C.-B., Wang, B.-F., Wu, J.-Z., Chong, K.L. & Zhou, Q. 2022*a* Suppression of flow reversals via manipulating corner rolls in plane Rayleigh–Bénard convection. *J. Fluid Mech.* **946**, A44.

Zhao, C.-B., Wu, J.-Z., Wang, B.-F., Chang, T., Zhou, Q. & Chong, K.L. 2024 Numerical study on the onset of global-scale flow from individual buoyant plumes: implications for indoor disease transmission. *Phys. Fluids* **36** (3), 035149.

Zhao, C.-B., Zhang, Y.-Z., Wang, B.-F., Wu, J.-Z., Chong, K.L. & Zhou, Q. 2022*b* Modulation of turbulent Rayleigh–Bénard convection under spatially harmonic heating. *Phys. Rev.* E **105** (5), 055107.